

## Article

# Modelling Aspects in the Simulation of the Diffusive Flame in A Bluff-Body Geometry

Alessandro Di Mauro <sup>1</sup>, Marco Ravetto <sup>1</sup>, Prashant Goel <sup>1</sup>, Mirko Baratta <sup>1,\*</sup>, Daniela Anna Misul <sup>1</sup>, Simone Salvadori <sup>1</sup>, Rainer Rothbauer <sup>2</sup> and Riccardo Gretter <sup>2</sup>

<sup>1</sup> Department of Energy, Politecnico di Torino, 10129 Torino, Italy; alessandro.dimauro@polito.it (A.D.M.); marco.ravetto@studenti.polito.it (M.R.); prashant.goel@polito.it (P.G.); daniela.misul@polito.it (D.A.M.); simone.salvadori@polito.it (S.S.)

<sup>2</sup> Convergent Science GmbH, 4040 Linz, Austria; rainer.rothbauer@convergecfcd.com (R.R.); riccardo.gretter@convergecfcd.com (R.G.)

\* Correspondence: mirko.baratta@polito.it; Tel.: +39-011-090-4484

**Abstract:** Gas turbines are expected to play a key role in the energy production scenario in the future, and the introduction of carbon-free fuels is fundamental for the development of a sustainable energy mix. The development of a reliable numerical model is thus fundamental in order to support the design changes required for the burners. This paper presents the results of a numerical investigation on a turbulent, diffusive, combustion test case, with the purpose of identifying the best compromise between accuracy and computational cost, in the perspective of the model application in real, more complex, geometries. Referring to a test case has two main advantages. First, a rather simple geometry can be considered, still retaining a few peculiar flow features, such as recirculation vortices and shear layers, which are typical of real applications. Second, the experimental setup is much more detailed than in the case of real turbines, allowing a thorough model validation to be performed. In this paper, the Standard 2-equations  $k-\epsilon$  model and the Speziale-Sarkar-Gatski Reynolds Stress Model are considered. Moreover, both the FGM combustion model and the detailed chemistry model are used, coupled with two chemical reaction mechanisms, and their results are compared. Finally, a standard and an enhanced near-wall approach are employed to solve the transport equations close to the walls. The results show a good agreement in the temperature distribution at the axial positions corresponding to the experimental measurements. Overall, the standard wall function approach for describing the near-wall flow proved to be more effective at increasingly higher distances from the jet centre. Such differences are related to the formulations employed by the two near-wall approaches, which led to changes in the predicted flow field around the fuel jet. Finally, the adoption of a reaction mechanism describing in detail the species concentration is mandatory whenever the reliable prediction of the NO<sub>x</sub> formation is of primary importance. The conclusion reached in this paper can be helpful for the development of reliable and cost-effective CFD models of turbine combustors.

**Keywords:** CFD; turbulent combustion; diffusive flame; pollutant emission modelling; gas turbines



**Citation:** Di Mauro, A.; Ravetto, M.; Goel, P.; Baratta, M.; Misul, D.A.; Salvadori, S.; Rothbauer, R.; Gretter, R. Modelling Aspects in the Simulation of the Diffusive Flame in A Bluff-Body Geometry. *Energies* **2021**, *14*, 2992. <https://doi.org/10.3390/en14112992>

Academic Editors: Antonio Andreini and Lorenzo Mazzei

Received: 13 April 2021

Accepted: 17 May 2021

Published: 21 May 2021

**Publisher's Note:** MDPI stays neutral with regard to jurisdictional claims in published maps and institutional affiliations.



**Copyright:** © 2021 by the authors. Licensee MDPI, Basel, Switzerland. This article is an open access article distributed under the terms and conditions of the Creative Commons Attribution (CC BY) license (<https://creativecommons.org/licenses/by/4.0/>).

## 1. Introduction

Turbulent combustion is surely one of the most challenging tasks for modern engineering applications, especially in industrial applications where fast and accurate results are of paramount importance. As a matter of fact, gas turbines are expected to still play a non-negligible role in the energy production scenario in the future, especially if coupled with the introduction of carbon-free fuels such as green hydrogen and bioliquids [1,2]. The development of a reliable numerical model is thus fundamental in order to support the design changes required for the burners, starting from the well-established technology for natural gas combustion.

Reynolds Averaged Navier Stokes (RANS) equations, coupled with various closure models, have been used extensively to predict flow structures and combustion processes,

both for simplified and complex geometries [3]. A fundamental advantage in the use of RANS-based models is the easily manageable computational time, which represents the main reason that drives industries in adopting such models. Various models have been proposed to account for turbulent combustion and its related phenomena (e.g., heat release and density fluctuations). Particularly, different basic concepts have been exploited—namely, flame sheet approximation [4], full or partial equilibrium [5] and laminar flamelet burning [6]. Reduction techniques are also very popular in engineering applications, since they can achieve good predictions in manageable computational times. Other, more complex models, accounting for detailed chemical kinetics, are available. These latter are capable of accurate performances even for transient phenomena, such as flame extinction and ignition. Nonetheless, the computational effort required to employ these kinds of models is large, and their industrial applications are still difficult.

Bluff-body flows and flames can be considered as valid and reliable test cases for model validation. Indeed, a complex recirculation zone, quite similar to the ones generated in more complex geometries, can be found in these cases. Moreover, the experimental setup is much more detailed than in the case of real turbines, allowing a thorough model validation to be performed. Experimental data are available for bluff-body flows and flames for different fuels and flow conditions [7–9]. Various attempts to model such flames have already been documented in the literature [10–13]. Large Eddy Simulations (LES) have also been performed with promising results for vortex visualization and vibration phenomena [14].

In the present study, two experimental test cases [15] are employed as benchmarks to validate both the turbulence and combustion models by means of RANS steady-state simulations and CONVERGE commercial software. Particularly, the Standard 2-equations  $k-\epsilon$  (Std  $k-\epsilon$ ) and Speziale-Sarkar-Gatski Reynolds Stress Model (SSG-RSM) are analysed, and their performances are assessed. Moreover, two combustion models of different complexities are coupled with two chemical reaction mechanisms, and their results are compared. Finally, two near-wall approaches are employed to solve the involved transport equations. Even though more complex and accurate turbulence closure approaches (i.e., LES) could provide an overall better agreement with the experimental results [16], the RANS model was selected in this paper to provide a sound basis for design-oriented applications on real gas turbine combustors. The main novelty of this study is the combination of differently detailed chemical kinetics solvers and reaction mechanisms, along with two near-wall approaches, to prove the validity and consistency of the employed simulation strategy.

Interesting results and insights were found, especially regarding the ability of the combustion models to predict pollutant mass fractions. The present study was conceived as a first step in the research activities of the authors in the field of diffusive combustion simulation. The conclusions reached in this paper can thus be a useful reference for the development of reliable and cost-effective CFD models of real, more complex gas turbine combustors, which can be a valuable support to the design of fuel-flexible burners of new, as well as of existing, turbines.

## 2. Test Cases

Two sets of data from the Sydney University bluff-body burner database were chosen as the experimental reference to evaluate the performance of the models under investigation [13]. The measurements were conducted at the Combustion Research Facility, Sandia National Laboratory, Livermore, CA, USA. More details on the experimental setup, error estimates and spatial resolution for this experiment have been published elsewhere [17–19]. A burner schematic is proposed in Figure 1. The bluff-body has an outer diameter of  $D_B = 50$  mm and a jet diameter of  $D_j = 3.6$  mm. Even though a square-shaped co-flow air tunnel was used in the experimental setup, it was replaced by a cylinder of 600 mm in diameter in the computational domain. This choice was motivated by the opportunity of

introducing a cylindrical symmetry in the model and justified by the negligible influence of this modification on the flow in the vicinity and around the flame region.

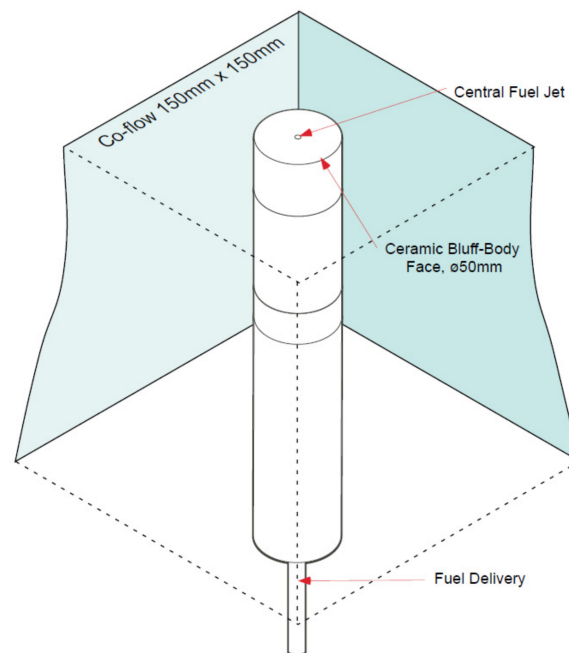


**Figure 1.** Sydney University bluff-body burner schematic [15].

As already stated, two experimental cases were reproduced in this study. The first one was a nonreactive jet, composed of air, which was considered for the turbulence model validation. Then, a reactive flame, featuring a mixture of 50% CH<sub>4</sub> and 50% H<sub>2</sub> as the fuel and oxidizing air as the co-flow, was considered. This experiment is denoted as “HM1 flame” in the Sydney database.

The main boundary conditions of the case study are available from the Sydney University database and are reported in Table 1. for the two experiments. It is worth noticing that a fully developed velocity profile was imposed as the inlet boundary condition so as to match the bulk velocity reported in the reference.

**Table 1.** Boundary conditions.

Location	Boundary Condition	Value
	Nonreactive Jet	
Co-flow inlet	Bulk velocity	20 m s <sup>-1</sup>
Jet inlet	Bulk velocity	61 m s <sup>-1</sup>
Outlet plane	Pressure/Temperature	1 bar/300 K
Bluff-body wall	Temperature	Adiabatic
	“HM1 flame”	
Co-flow inlet	Bulk velocity	40 m s <sup>-1</sup>
Jet inlet	Bulk velocity	118 m s <sup>-1</sup>
Outlet plane	Pressure/Temperature	1 bar/300 K
Bluff-body wall	Temperature	Adiabatic

### 3. Numerical Method

In the present application, the Reynolds Averaged Navier–Stokes equations were adopted as the governing equations; two methods of closure were considered—namely, the Std k- $\epsilon$  and the SSG-RSM. As mentioned above, the numerical model was developed within CONVERGE. The latter is a general-purpose CFD code distributed and licensed by Convergent Science.

The Monotonic Upstream-centred Scheme for Conservation Laws (MUSCL) spatial discretisation scheme, which is second-order accurate [20], was implemented for the fluxes definition, as will be detailed in the next section. Moreover, two combustion models were compared in this study, along with two reaction mechanisms—namely, the SAGE-detailed chemical kinetics solver (SAGE) [21] in conjunction with the GRI-Mech 3.0 [22] reaction mechanism and the Flamelet Generated Manifold (FGM) [23] in combination with the CRECK [24] reaction mechanism. An introduction to these latter ones is given in Sections 3.2–3.4.

### 3.1. MUSCL Numerical Scheme

A blend of second-order upwind and reconstructed central difference spatial discretisation was employed by the MUSCL scheme to compute the convection term of the governing equations. The cell faces values of a certain quantity  $\varphi$  were estimated through a linear reconstruction method; then, the cell value was computed with both a central differencing scheme and second-order upwind scheme; finally, the two values were blended using the following relation:

$$\varphi_{f, muscl} = (1 - \beta) \cdot \varphi_{f, ru} + \beta \cdot \varphi_{f, rcd} \quad (1)$$

where  $\varphi_{f, muscl}$  is the final computed quantity,  $\varphi_{f, ru}$  is the quantity computed through the second-order upwind discretisation,  $\varphi_{f, rcd}$  is the quantity computed through the central differencing scheme and  $\beta$  is the blending factor.

It is worth pointing out that the MUSCL discretisation scheme was combined with a slope limiter [25] so as to avoid model instability, which might be caused by unphysical local maxima or minima.

### 3.2. SAGE Detailed Chemical Kinetics Solver

The SAGE solver is included in the CONVERGE package and represents an effective tool for the calculation of species concentration and reaction rates, taking convective and diffusive transport into account. SAGE was employed in this study to solve the mass and energy conservation equations for any given cell of the domain. Particularly, these latter are the following:

$$\frac{d[X_j]}{dt} = \dot{\omega}_j \quad (2)$$

$$\frac{dT}{dt} = \frac{\dot{Q} - \sum_j (\bar{h}_j \dot{\omega}_j)}{\sum_j ([X_j] \bar{c}_{p,j})} \quad (3)$$

where  $[X_j]$  and  $\dot{\omega}_j$  are the molar concentration and net production rate of species  $j$ , respectively, and  $T$ ,  $V$  and  $\dot{Q}$  are the temperature, volume and heat transfer rate of a given cell, respectively. Finally,  $\bar{h}_j$  and  $\bar{c}_{p,j}$  are the molar specific enthalpy and molar constant pressure-specific heat of species  $j$ . A detailed description of the system of equations to be solved was provided in references [21,26]. The above equations were solved at each time-step, and the species were updated accordingly. However, the temperature computed through Equation 3 was not used to update the cell temperature at each iteration. Instead, this latter was updated once the chemistry calculation converged by using the computed species concentrations.

### 3.3. Flamelet Generated Manifold

The SAGE solver, coupled with a suitable reaction mechanism, is intrinsically the most accurate simulation method for reactive flows. However, the target of this work was to define the best possible trade-off between accuracy and computational time, in view of the application of the method to a real gas turbine diffusive combustor. Hence, the FGM model was also applied in this study. In fact, in the gas turbine reactive flows, a large set of equations was raised due to the high number of species involved, and the CPU load

was further increased by a very large cell count. Moreover, the equations were strongly coupled by the source chemical source terms. The numerical solution of the set of fully coupled governing equations for the reactive flows was computationally expensive.

Standard reduction techniques are based on the assumption that the majority of the species is in a steady state. In this manner, it is possible to reduce the species mass fraction conservation equations to a balance between the chemical rate of production and consumption. However, this procedure leads to poor approximations in regions where transport and diffusion are of considerable importance (i.e., colder regions). Far better results can be achieved by accounting for the major transport processes. These latter are considered well-represented by 1D flames. The evolution of all the species mass fractions  $Y_i$  was approximated by the one-dimensional Equation (4). This latter was defined along the curve  $x(s)$  parametrized by the arc length  $s$  and locally perpendicular to the iso-surface of the species mass fraction under analysis.

$$m \frac{\partial Y_i}{\partial s} - \frac{\partial}{\partial s} \left( \frac{1}{Le_i} \frac{\lambda}{c_p} \frac{\partial Y_i}{\partial s} \right) = \omega_i^+ - \omega_i^- + P_i \quad (4)$$

where  $m$  is a constant mass-flow rate per unit area,  $Le$  is the Lewis number,  $\lambda$  is the thermal conductivity and  $c_p$  is the specific heat at constant pressure. Furthermore,  $\omega_i^+$  and  $\omega_i^-$  are the production and consumption parts of the chemical source term. Finally,  $P_i$  is a perturbation term gathering a multidimensional and transient effect. This latter is neglected, since it is believed to be small in most situations, compared to the other terms.

The FGM is based on the hypothesis that the local flame behaviour is laminar; however, the turbulence effect is introduced through the description of the flame wrinkling and stretching effects. The FGM model allows the combustion to be reduced to a set of similar equations that can be solved before the actual simulations. The solution to these equations is the so-called flamelet. The results coming from the just-mentioned solving procedure are stored in a 2D look-up table that can be accessed throughout the simulations.

The FGM combustion model is believed to also correctly predict turbulence/combustion interactions in case of hydrogen flames [27].

### 3.4. GRI-Mech 3.0 and CRECK Reaction Mechanisms

For both SAGE and FGM models, a reaction mechanism is needed as the input. Different mechanisms can be found in the literature, which differ in the number of species and reactions involved. A more detailed reaction mechanism is expected to describe the actual chemical kinetics of the process more accurately. Therefore, they most likely allow more accurate predictions of the temperature and species mass fractions to be achieved. Nevertheless, a more complete description of the chemical kinetics is linked with an inevitable surge in computational time. The present study should be considered as the starting ground for a future and more realistic, yet complex, application to a real gas turbine combustor. In this perspective, the increase in computational effort has been carefully considered. Even though it could have been possible to employ a detailed reaction mechanism in combination with the SAGE solver in the present study, a similar approach would not be feasible for future applications. Within this framework, the GRI-Mech 3.0 reduced reaction mechanism was used with the SAGE solver. Instead, the detailed CRECK reaction mechanism was employed in combination with the FGM model.

The GRI-Mech 3.0 features 53 species and 325 reactions with associated rates and thermodynamic data, whereas the CRECK contains the rates and thermodynamic data for 159 species and 2459 reactions. Moreover, both the Zeldovich and prompt  $\text{NO}_x$  production processes are accounted for in either reaction mechanism.

## 4. Nonreactive Flow Simulation

As stated above, the first analyses were carried out with steady-state, nonreactive simulations. For brevity, they will be referred to as “cold-flow” simulations. A brief

description of the computational domain and of the grid control techniques is presented below, followed by the main results.

#### 4.1. Computational Domain and Grid Control

Due to the fairly simple problem configuration and the acceptable associated CPU load, the entire geometry was simulated in this case, without introducing any symmetry plane boundary conditions. The last section of the bluff-body and the co-flow case are modelled (Figure 2).

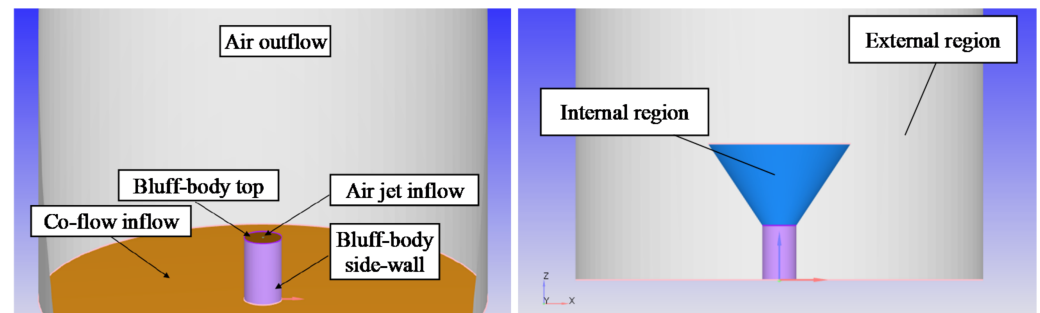


**Figure 2.** Nonreactive flow simulation computational domain.

An orthogonal cartesian hexahedral grid was employed in the cold-flow simulations. The grid was automatically generated by CONVERGE, and the grid size was controlled by means of two available tools—namely, “fixed embedding” and “Adaptive Mesh Refinement” (AMR). They were employed to refine the base grid, which had a fixed base grid size (16 mm in the present application). The refinement equation for both fixed embeddings and AMR is the following:

$$dq_{embedded} = \frac{dq_{base}}{2^n} \quad (5)$$

where  $dq_{base}$  is the base grid size in any of the three cartesian direction,  $dq_{embedded}$  is the grid size after the refinement and  $n$  is the user-defined embed scale.

A grid sensitivity analysis was performed prior to the numerical campaign. It was found that the CFD results were mainly affected by the grid size in the jet region and around it. More specifically, the results did not show sensible dependence on the mesh size once a cell dimension below 0.3 mm was used. It was also essential to guarantee a spatial extension of the refinement, so as to include the region where the shear effect between the jet and the surrounding air occurred. The best trade-off between accuracy and CPU requirement, with specific reference to the dimension of the refinement region, was defined by taking advantage of the Adaptive Mesh Refinement (AMR) feature. The AMR is a peculiar and flexible facility embedded in CONVERGE software, which is useful to reduce the numerical errors for the variables such as velocity, temperature, turbulence or species mass fraction. The AMR algorithm decreases the cell size on the basis of the estimation of the variable gradients and of the comparison to user-defined thresholds. A thorough description of the resulting grid is proposed in Table 2. After the simulations were performed, the cell count was found to be approximately 460,000 and 520,000 for the Std k- $\epsilon$  model and the SSG-RSM model, respectively.

**Table 2.** Grid control details for the nonreactive flow simulations.

Type	Location	Embed Scale/Grid Size
Fixed Embedding	Around the jet	5/0.25 mm
Fixed Embedding	Around the bluff-body	2/2.00 mm
AMR	Internal region	5/0.25 mm
AMR	External region	2/2.00 mm

## 4.2. Results

Cold-flow simulations were performed employing both the Std  $k-\epsilon$  and the SSG-RSM turbulence model. Moreover, the MUSCL numerical scheme was used to solve the convection terms in the governing equations. As a preliminary analysis, not reported in the paper for the sake of conciseness, a calibration over the  $C_{\epsilon 1}$  constant was performed, and the value  $C_{\epsilon 1} = 1.6$  was found to better reproduce the experimental results. As a matter of fact, the literature confirms that the latter value was a good choice for this type of problem [13,28,29].

The cold-flow simulations results were therefore proposed in what follows for both the aforementioned models using the MUSCL numerical scheme and  $C_{\epsilon 1} = 1.6$ .

The axial velocity profiles against the normalized distance from the axis, along with the radial velocity profiles, are presented in Figure 3 for four axial distances from the jet exit plane—namely, 1.5 mm, 10.0 mm, 20.0 mm and 30.0 mm. Moreover, two sets of measurement repetitions were available for the discussed setup and are both proposed in the graphs below.

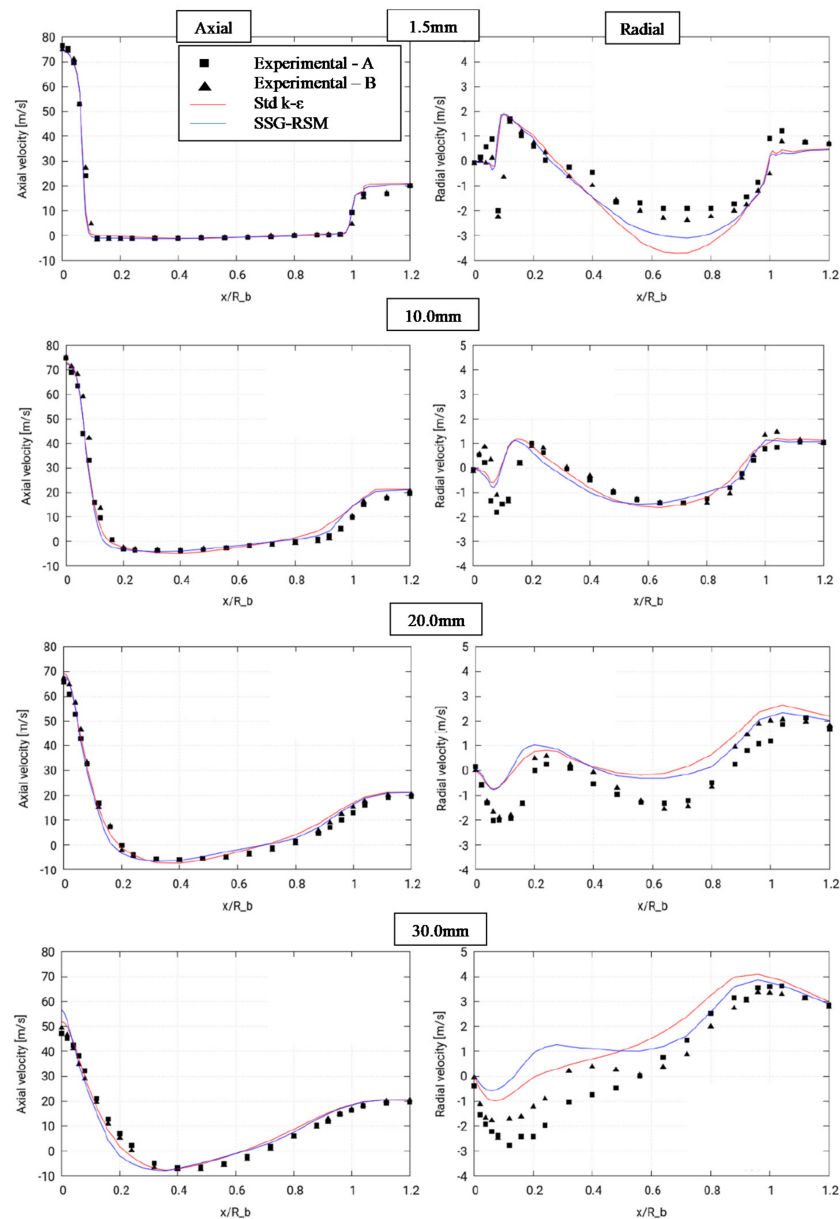


**Figure 3.** Axial and radial velocity profiles at increasing axial distances. Nonreactive flow simulations. Complete experimental data available at reference [15].

The axial velocities were correctly predicted by the models for all the axial positions, with some minor deviations at a 30.0-mm distance. More specifically, the maximum deviation from the experimental results was achieved by the RSM model at a 30.0-mm axial distance and 0.2 relative radial distance (i.e., 0.2 diameters far from the centre line) which corresponded to the end of the jet tube (Figure 1). In such a case, the Mean Absolute Percentage Error (MAPE) was around 8%. Overall, the MAPE factor ranged from 5.2% to 12% for the Std  $k$ - $\epsilon$  model and from 5.2% to 15% for the RSM, thus confirming a comparable prediction capability from these models, given also that the trend was well-reproduced at all the locations.

The radial velocity behaviour was qualitatively well-predicted by the models; however, larger deviations were present, and the MAPE varied in the 40–90% range. It should be highlighted, however, that the absolute values of these velocities were far smaller than the axial ones, resulting in larger relative deviations even for small errors. Moreover, it can be seen that, especially at a 30.0-mm distance, the two experimental readings presented non-negligible differences from each other, suggesting that the associated uncertainty was quite higher than for the axial velocity.

Both the turbulence models analysed were found to accurately replicate the axial and radial velocities; in fact, equivalent performances in terms of the prediction accuracy were registered. However, since the RSM model gave rise to a much higher computational effort (i.e., 12 h on four processors) with respect to the standard  $k$ - $\epsilon$  model (i.e., 5-and-a-half hours on four processors), the latter was chosen to carry on the reactive flow simulations.

## 5. Reactive Flow Simulation

The second set of analyses was performed on the steady-state, chemically reactive flows. These will be referred to as “hot-flow simulations”.

Once again, the computational domain is firstly presented, along with the grid size control techniques; then, the results are shown and discussed.

### 5.1. Computational Domain and Grid Control

Contrarily to cold-flow simulations, the domain was reduced to account for the increased computational effort coming from the combustion model. In fact, only a 90° sector of the domain was modelled, exploiting the geometrical symmetry of the problem. In this regard, periodic boundary conditions were employed at two corresponding planes of the domain (Figure 4).

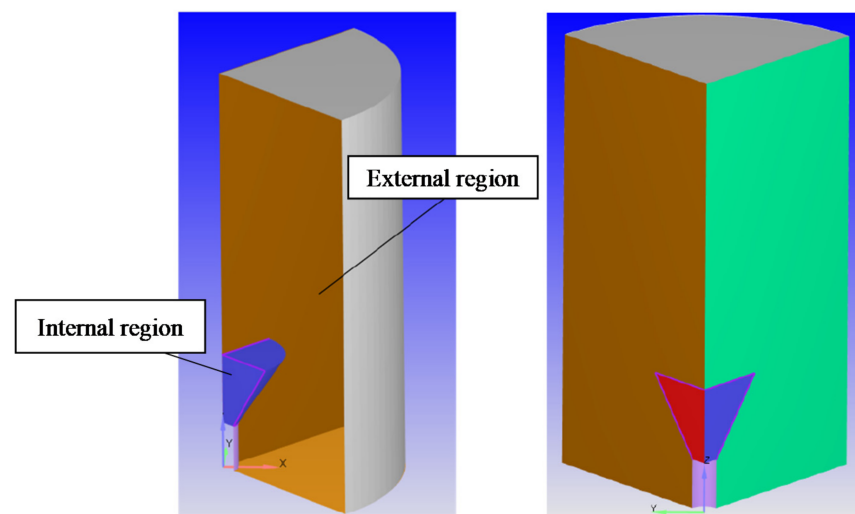


Figure 4. Reactive flow simulations of the computational domain.

Similar to the previous case, the grid size was controlled using two fixed embeddings and two AMR regions starting from a base mesh of 16 mm. After a few preliminary

tests, in which some differences were found with respect to the “cold flow” simulation results, the fixed embedding regions were enlarged in the reactive flow case. The general characteristics of both the fixed embeddings and the AMR regions were the same as for the cold-flow simulations (Table 2). An example of the grid obtained after the AMR refinement is presented in Figure 5: A Y-plane slice of the entire domain is shown, alongside an enlargement of the zone described in the graphs in the following sections. It is worth noticing that increasing the overall number of cells led to no substantial changes in the zone of interest in the study; however, the results of the just-mentioned analysis was not presented in the present work for the sake of conciseness.

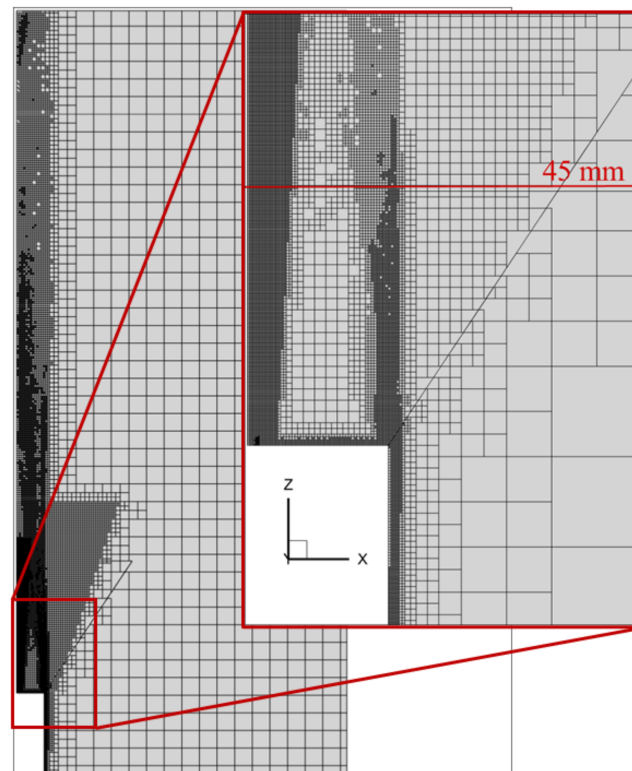


Figure 5. Example of the grid obtained after AMR refinement.

## 5.2. Results

Two combustion models were tested—namely, the SAGE and FGM models (Section 3). Due to the different computational efforts required by the SAGE and FGM combustion models, different reaction mechanisms were coupled to the latter: the more complex SAGE model was used in combination with the GRI-Mech 3.0 reaction mechanism, while the FGM model was employed with the more complete CRECK reaction mechanism. As already stated, exploiting the SAGE model together with the CRECK reaction mechanism, although possible in the present study, would have led to a nonmanageable computational time in the future application of gas turbine burners.

Moreover, two approaches regarding the near-wall treatment have been studied: standard wall function and enhanced wall treatment. Briefly, the first is employed whenever it can be assumed that the first cell near the wall lies in the log-law region of the flow; a logarithmic relation is therefore applied by the code to compute the velocities in the wall-adjacent cell. Conversely, an enhanced wall treatment could theoretically be used for any near-wall situation, regardless of the  $y^+$  value of the first cell. Indeed, a blended formulation was used to compute the value of the turbulent dissipation rate  $\varepsilon$  at the wall-adjacent cell:

$$\varepsilon = \exp(-\Gamma_\varepsilon)\varepsilon_{visc} + \exp\left(-\frac{1}{\Gamma_\varepsilon}\right)\varepsilon_l \quad (6)$$

where  $\Gamma_\varepsilon$  is a blending parameter, and  $\varepsilon_{visc}$  and  $\varepsilon_l$  are the computed viscosities, assuming the first cell is located in the viscous sublayer and the log-law layer, respectively.

First, the results of the simulations involving SAGE combustion model with GRI-Mech 3.0 reaction mechanism are reported hereafter, and the prediction accuracy of both the standard wall function and enhanced wall treatments are compared. Then, similar results are presented for the FGM combustion model with CRECK reaction mechanism.

The axial velocity profiles obtained with SAGE coupled to the GRI-Mech 3.0 mechanism are presented in Figure 6 at four axial distances from the jet exit plane—namely, 5.0 mm, 13.0 mm, 30.0 mm and 45.0 mm. The prediction accuracy of the radial velocities was found to be comparable with the one obtained in the cold-flow simulations (MAPE  $\approx$  45–90%). Furthermore, given the absence of any significant radial flow induced by the fuel and the air, the values of the radial velocities were close to zero at every measurement location. Thus, they were omitted for the sake of conciseness.

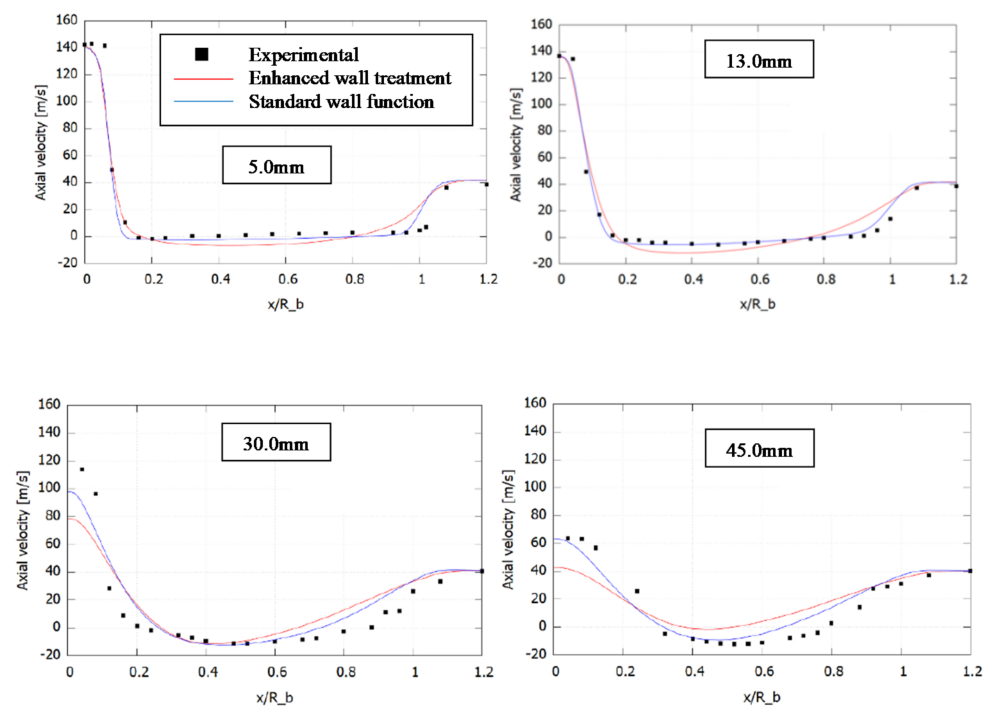


**Figure 6.** Axial velocity profiles at increasing axial distances. SAGE/GRI-Mech 3.0. Complete experimental data available at reference [15].

It is clear from the results that the standard wall function seemed to better predict the velocity profile. This tendency was more apparent as the distance from the jet exit plane increased. It is worth pointing out that the calibration procedure conducted upon  $C_{\varepsilon 1}$  was performed by employing the standard wall function. It was then possible that a different  $C_{\varepsilon 1}$  value could be more suitable for the enhanced wall treatment approach.

The temperature profiles at the four axial distances (i.e., 5.0 mm, 13.0 mm, 30.0 mm and 45.0 mm) are presented in Figure 7, along with the NO mass fraction in Figure 8. The experimental data dispersion (i.e., raw data) [15] is also available for the temperature profiles.

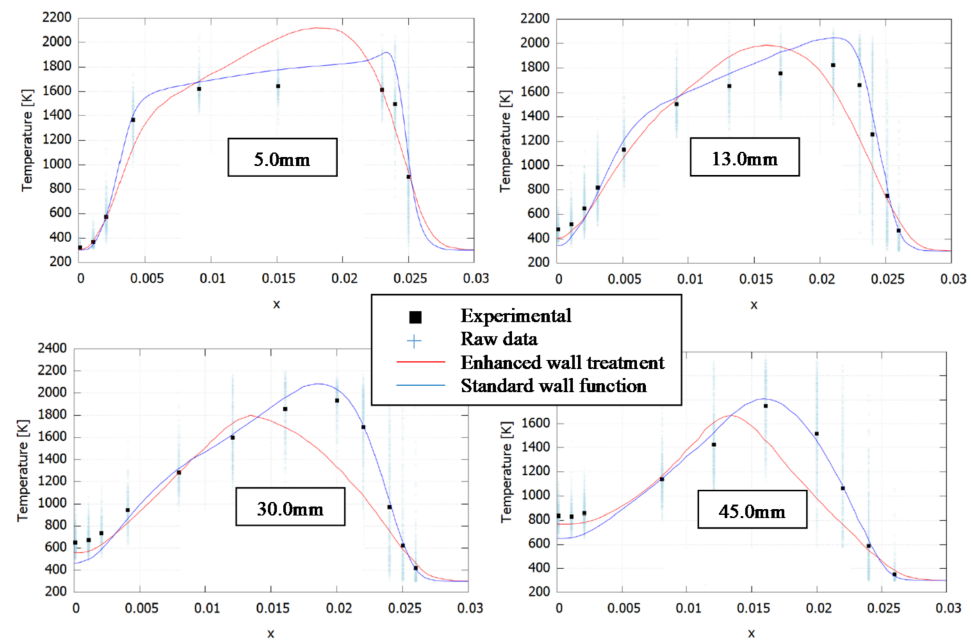


**Figure 7.** Temperature profiles at increasing axial distances. SAGE/GRI-Mech 3.0. Complete experimental data available at reference [15].

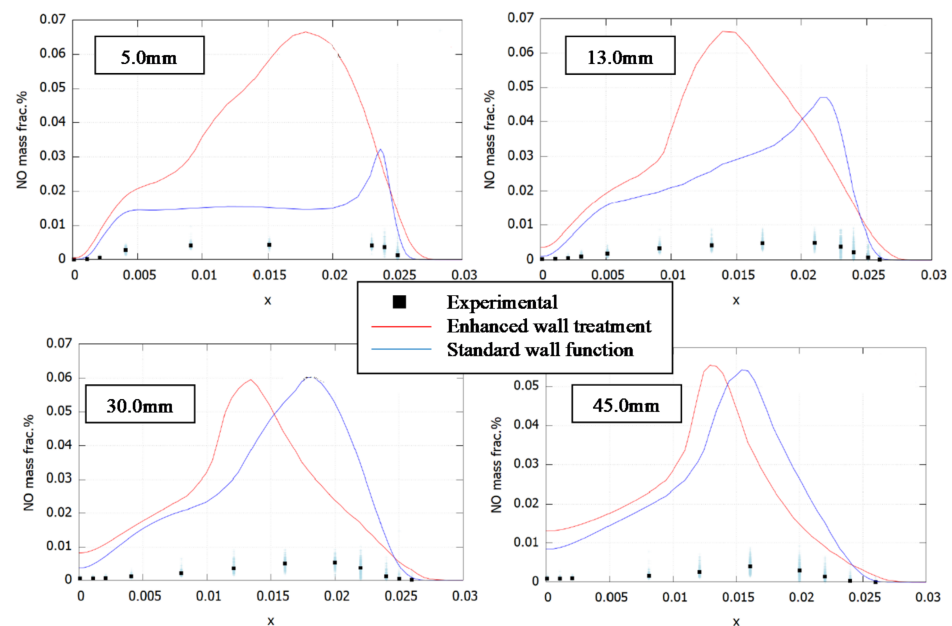


**Figure 8.** NO mass fraction profiles at increasing axial distances. SAGE/GRI-Mech 3.0. Complete experimental data available at reference [15].

The results clearly show that the enhanced wall treatment was able to better predict the temperature nearer the jet; however, the majority of the profile was affected by larger deviations from the experimental measurements with respect to the standard wall function. Overall, the MAPE index was around 6% for the standard wall function at all the locations, whereas it ranged from 6% or 7% to 15% for the enhanced one. This behaviour was directly linked to the different predictions of the species mass fraction, which were obtained with the two wall functions. The distribution of the fuel species mass fraction is reported in Figure 9. at a 5.0-mm axial distance. A more precise prediction of the fuel species mass fraction (i.e.,  $\text{CH}_4$  and  $\text{H}_2$ ) near the centre line of the jet was achieved by the enhanced wall treatment, whereas an overall better prediction was provided by the standard wall

function. This was consistent with the differences already observed for the velocity and could justify the changes in species concentrations.

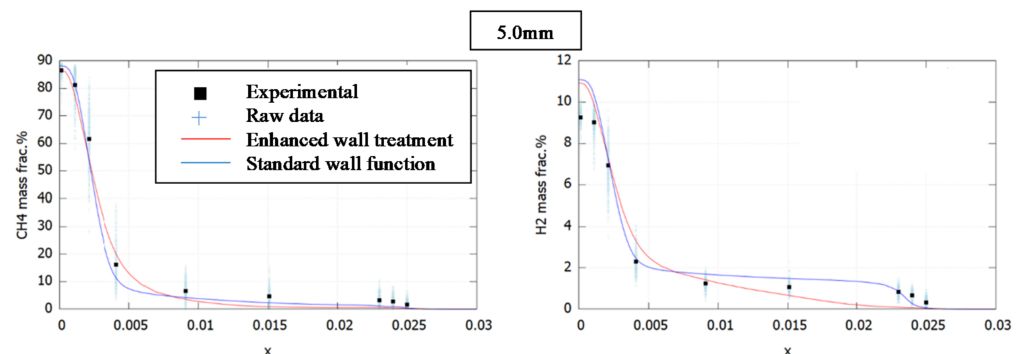


**Figure 9.** Fuel species mass fraction profiles at a 5.0-mm axial distance. SAGE/GRI-Mech 3.0. Complete experimental data available at reference [15].

Such differences were related to the formulations employed by the two near-wall approaches, which were discussed above. A thorough explanation will be proposed together with the comments to the FGM/CRECK combustion model.

The NO mass fraction profiles were strongly overestimated by the SAGE/GRI-Mech 3.0 combustion model. This was probably related to the GRI-Mech 3.0 mechanism, thus suggesting that a more appropriate mechanism should be considered whenever the accurate prediction of NO<sub>x</sub> is of primary importance.

Overall, both the approaches for near-wall treatment allowed satisfactory results to be obtained. Indeed, the numerical temperature distributions were almost always within the range given by the dispersion of the raw data of the experimental measurements, and the overall model was believed to be suitable for future temperature predictive simulations. On the other hand, further improvements of the NO formation model are needed to better reproduce the experimental measurements.

Figures 10–16 report the results obtained with the FGM model, coupled with the CRECK mechanism. In particular, the axial velocities are shown in Figure 10. The behaviour of the axial velocity was well-predicted by both models, with no substantial changes with respect to the SAGE/GRI-Mech 3.0 computations. However, the standard wall function seemed to overestimate the jet velocity for the last axial distance (i.e., 45 mm,  $x/R_b$  below 0.1). Overall, the use of FGM and the CRECK reaction mechanism was found to increase the accuracy of the enhanced wall treatment predictions.

The aforementioned differences in the near-wall modelling approaches can be clearly noticed when looking at turbulence-related quantities. Particularly, in Figure 11, the turbulent viscosity  $\mu_t$  is depicted. Streamtraces are also present in the same graphs, allowing for the visualisation of the recirculation zone. As it is evident, the enhanced wall treatment predicted higher levels of  $\mu_t$  near the bluff body. As a consequence, the flow was more diffusive, causing the velocities to decay faster at the jet centre line and to spread more intensively (i.e., the changes in axial velocity were sharper in the standard wall function approach). Moreover, if the enhanced wall treatment was employed, the recirculation zone was driven at a lower location.

These considerations are also consistent with the computed turbulent kinetic energy,  $tke$ , in the same zone (Figure 12). A higher  $tke$  value can be appreciated to the right of the outer W isoline, which was generated within the boundary layer belonging to the co-flow inlet zone. Finally, the temperature levels are proposed in Figure 13, confirming once again the more diffusive behaviour due to the different computed turbulent-related quantities.

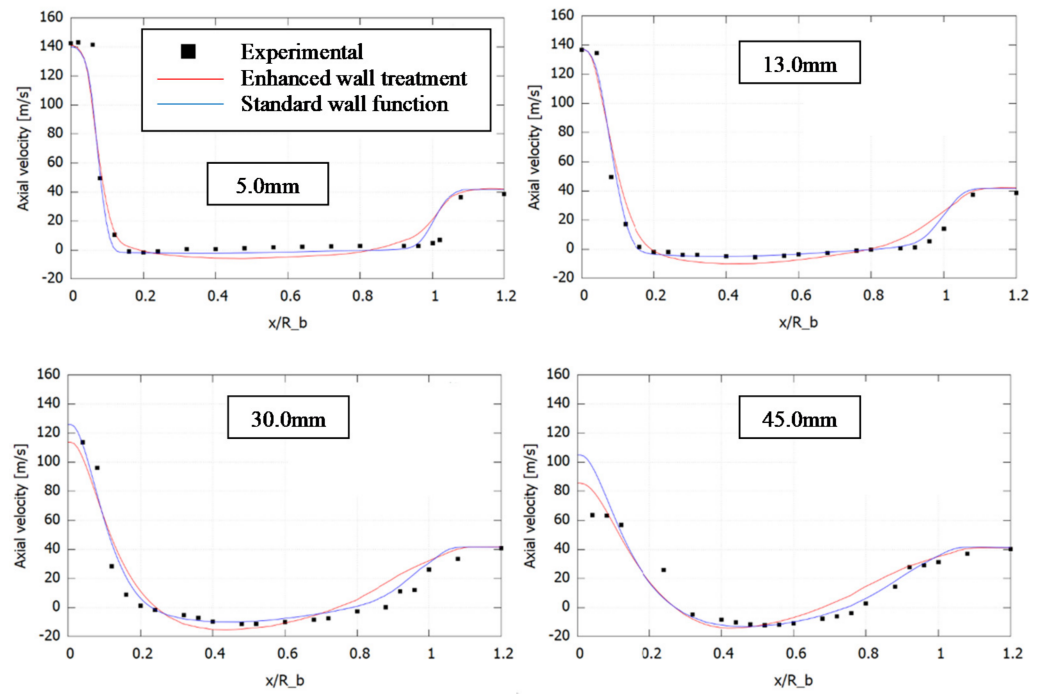


Figure 10. Axial velocity profiles at increasing axial distances. FGM/CRECK. Complete experimental data available at reference [15].

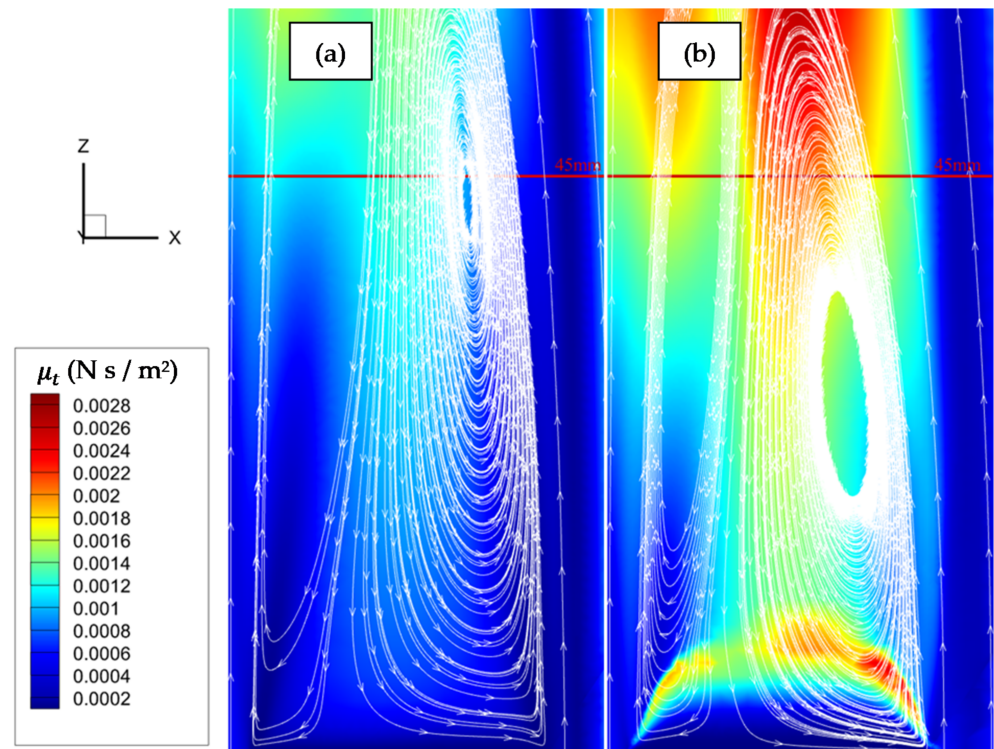
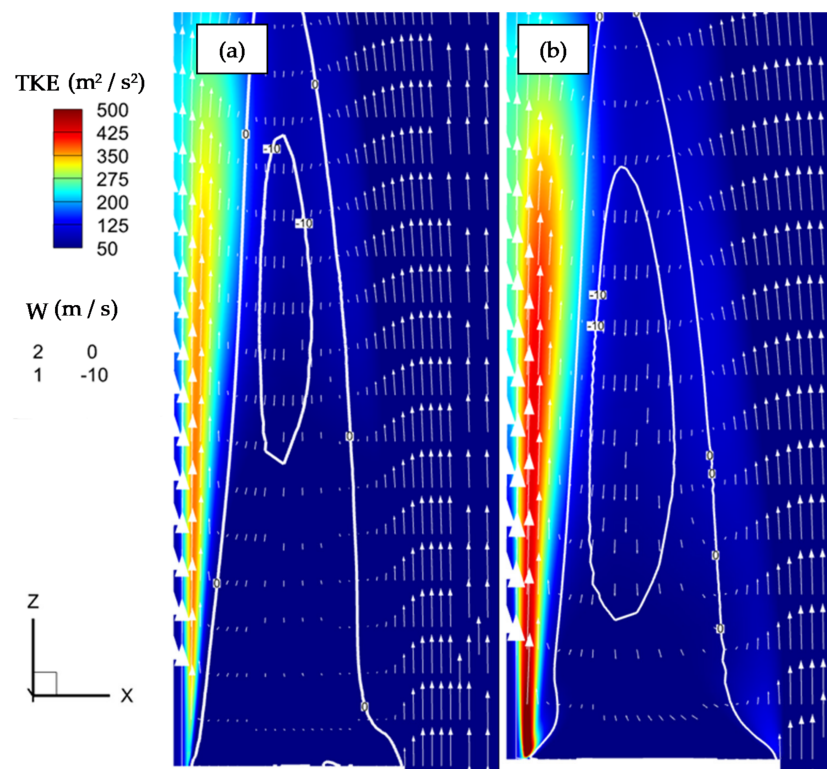
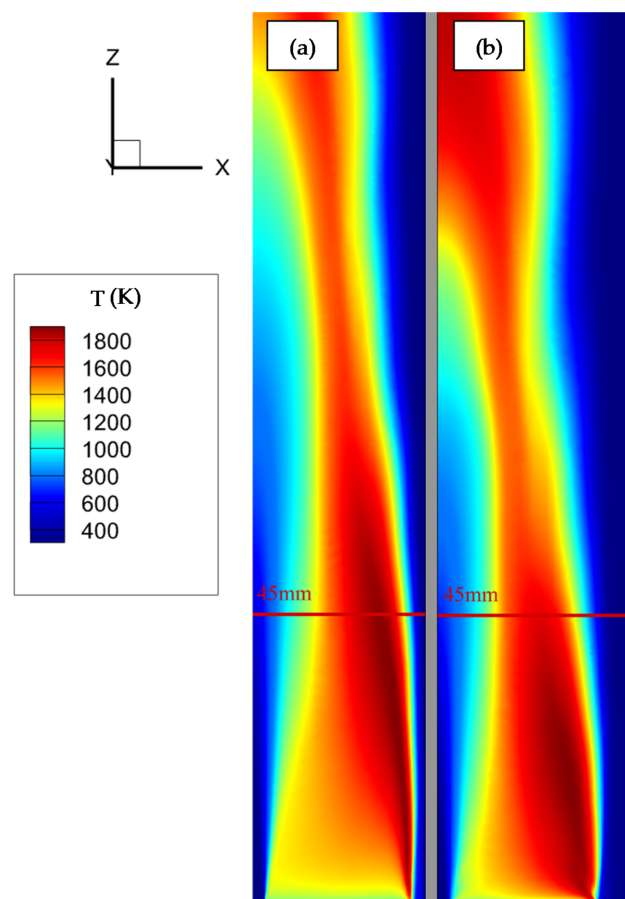


Figure 11. Turbulent viscosity and streamtraces. (a) Standard wall function. (b) Enhanced wall treatment.



**Figure 12.** Turbulent kinetic energy contours with axial velocity  $W$  isolines and tangent vectors. (a) Standard wall function. (b) Enhanced wall treatment.



**Figure 13.** Temperature contours. (a) Standard wall function. (b) Enhanced wall treatment.

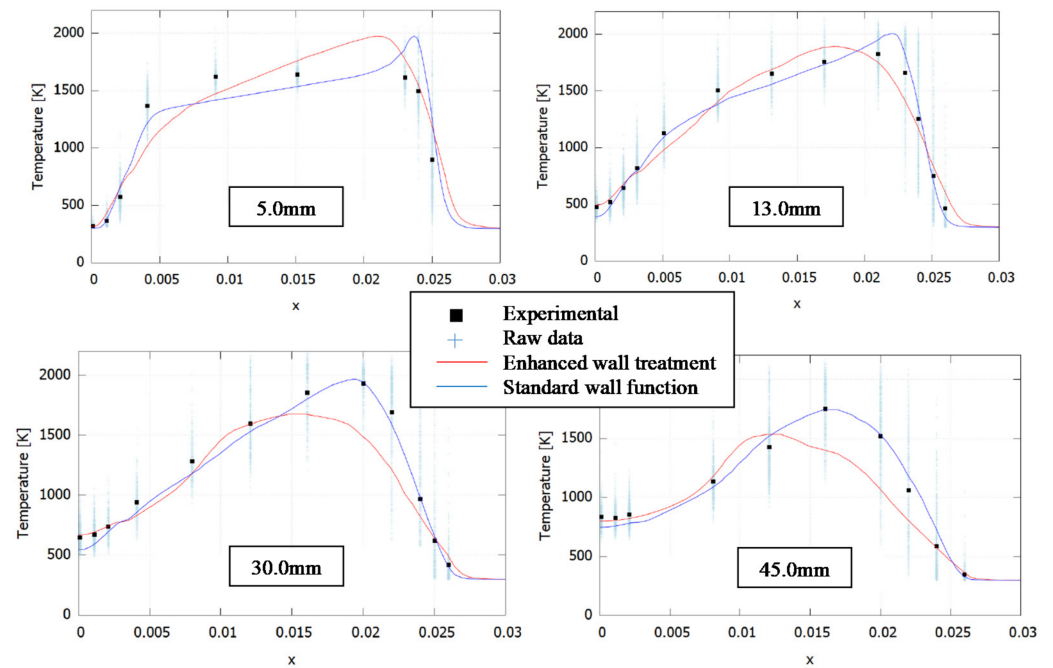


**Figure 14.** Temperature profiles at increasing axial distances. FGM/CRECK. Complete experimental data available at reference [15].

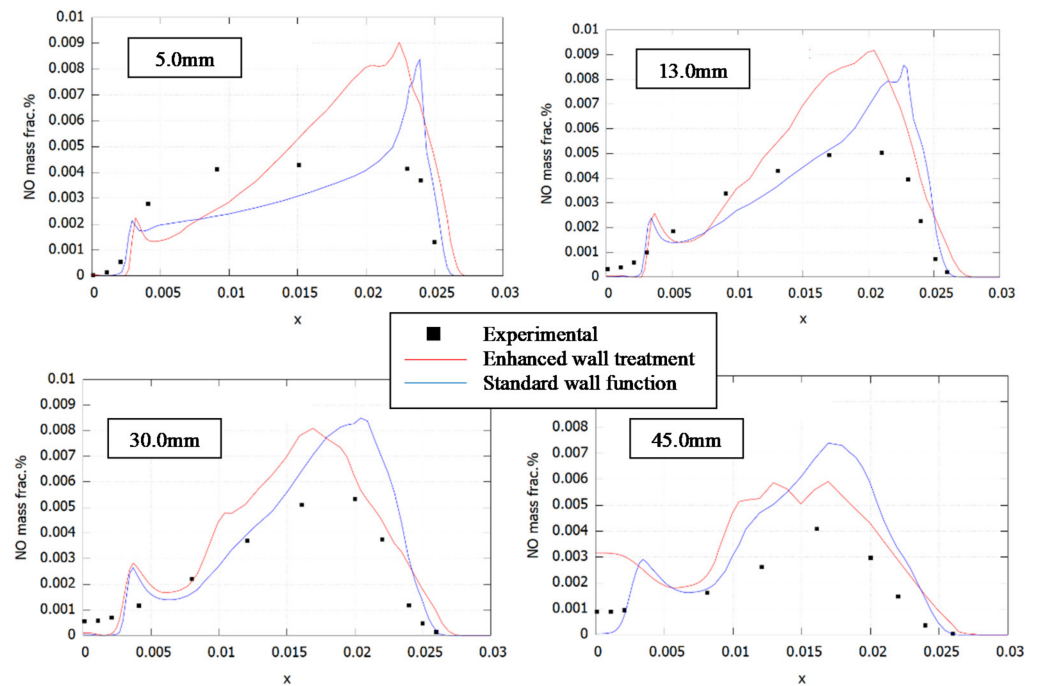


**Figure 15.** NO mass fraction profiles at increasing axial distances. FGM/CRECK. Complete experimental data available at reference [15].

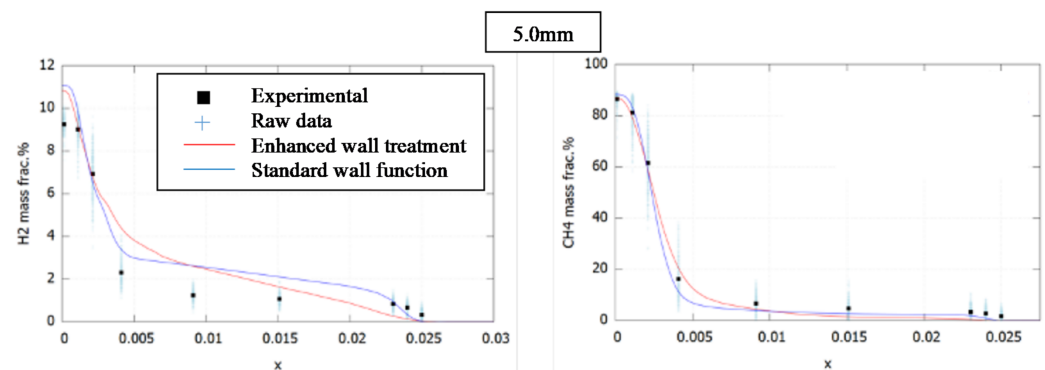


**Figure 16.** Fuel species mass fraction profiles at increasing axial distances. FGM/CRECK. Complete experimental data available at reference [15].

The results in terms of temperature distribution were quite similar to those in Figure 7, although a local overestimation was present at the radial positions between 0.02 m and 0.025 m, particularly for the standard wall treatment (blue curve). On the other hand, a higher average error was provided by the enhanced one (red curve) but with a more regular trend. Instead, the CRECK mechanism allowed a great improvement of the NO<sub>x</sub> results accuracy to be obtained. This is to be ascribed to the more detailed reaction mechanism, with specific reference to the modelling of the species involved in the nitrogen oxidation; indeed, the CRECK reaction mechanism has recently undergone a major update regarding the prompt production process [30]. On an average, the MAPE of NO<sub>x</sub> results were between 40% and 55% for the standard wall function and increased to 60–105% when the enhanced one was applied, hinting at the sole capability of estimating the NO<sub>x</sub> concentration order of magnitude. The larger deviations were found between  $x = 0.02$  and  $x = 0.025$  m, consistent with those already observed for the temperature. It is worth recalling that the bluff body had a radius of 25 mm; hence, the aforementioned zone was the one at which the co-flow air influence was stronger. This behaviour was probably due to errors of the model in high shear stress regions and might be due to the different descriptions of the co-flow boundary layer upstream of the fuel hole position. However, these errors are believed to retain a reduced relative importance in practical applications where the flow is guided and confined by the surrounding structures, thus constraining the boundaries and the size of the turbulent vortices. Finally, it is worth underlining that the results in Figure 15 confirm that a more appropriate mechanism than GRI-Mech 3.0 should be considered when NO<sub>x</sub> evaluation is of primary importance.

In conclusion, the FGM model, in conjunction with the CRECK reaction mechanism, is considered more reliable in the simulation of a diffusive steady-state flame, with specific reference to the NO mass fraction predictions, and it will therefore be selected for further analyses in the field of gas turbine burners.

## 6. Conclusions

The velocity, temperature and pollutant mass fraction distributions in the bluff-body stabilised flows were investigated in this work. Two turbulence models were validated over the nonreactive jet flow. Both tested turbulence models showed good agreement with the experimental results; therefore, the Std  $k-\epsilon$  was selected for the subsequent analyses due to the smaller computational effort required. The SAGE/GRI-Mech 3.0 combustion model was compared with the FGM/CRECK combustion model, employing two approaches for the near-wall regions.

Both the combustion models showed good agreement in replicating the temperature distribution at various axial positions. Overall, the standard wall function approach for describing the near-wall flow proved to be more effective at increasingly higher distances from the jet centre. Such differences are related to the formulations employed by the two near-wall approaches, which led to changes in the predicted flow field around the fuel jet.

Deviations from the experimental results were found regarding the temperature profile (and, consequently, in the NO distributions) at radial positions corresponding to the zone where the co-flow influence was stronger. This behaviour was especially evident for the standard wall function approach.

The FGM/CRECK combustion model showed far superior performances in reproducing the NO distribution at all the radial and axial positions with respect to the SAGE/GRI-Mech 3.0 model. This is believed to be related to the more complete description of the nitrogen oxidation processes in the CRECK reaction mechanism.

Overall, these conclusions can be applied to the diffusion flames governed by the shear effects and turbulent diffusion. The errors introduced in the modelling of the wall shear layers are believed to retain a reduced relative importance in practical applications where the flow is guided and confined by the surrounding structures, thus constraining the boundaries and the size of the turbulent vortices. The results can therefore be a useful reference for the development of reliable and cost-effective CFD models of real, more complex gas turbine combustors.

**Author Contributions:** Simulations: A.D.M., R.G. and M.R. Analysis: A.D.M., M.R., P.G., M.B., D.A.M., S.S., R.R., R.G. Writing: A.D.M. Supervision: P.G., M.B., D.A.M., S.S., R.R. and R.G. All authors have read and agreed to the published version of the manuscript.

**Funding:** This research received no external funding.

**Institutional Review Board Statement:** Not applicable.

**Informed Consent Statement:** Not applicable.

**Data Availability Statement:** The data is contained within this article.

**Acknowledgments:** Computational resources were also provided by HPC@POLITO (<http://hpc.polito.it>).

**Conflicts of Interest:** The authors declare no conflict of interest.

## Nomenclature

$C\epsilon_1$	Turbulent dissipation constant (-)
$\bar{c}_p$	Molar constant-pressure specific heat ( $\text{J K}^{-1} \text{mol}^{-1}$ )
$c_p$	Constant-pressure specific heat ( $\text{J K}^{-1} \text{kg}^{-1}$ )
$D_B$	Bluff-body outer diameter (m)
$D_j$	Bluff-body jet diameter (m)
$dq_{base}$	Base grid size (m)
$dq_{embedded}$	Grid size after fixed embedding refinement (-)
$\bar{h}$	Molar specific enthalpy ( $\text{J mol}^{-1}$ )
$Le$	Lewis number (-)
$m$	Mass-flow rate per unit area ( $\text{kg s}^{-1} \text{m}^{-2}$ )
$n$	Embed scale (-)
$P_i$	Perturbation term for species $i$ ( $\text{kg s}^{-1} \text{m}^{-2}$ )
$\dot{Q}$	Heat transfer rate (W)
$s$	Arc length variable (m)
$T$	Cell temperature (K)
$t$	Time (s)
$tke$	Turbulent kinetic energy ( $\text{m}^2 \text{s}^{-2}$ )
$V$	Cell volume ( $\text{m}^3$ )
$W$	Axial velocity ( $\text{m s}^{-1}$ )
$[X]$	Molar concentration ( $\text{mol m}^{-3}$ )
$Y$	Mass fraction (-)
Greek symbols	
$\beta$	MUSCL blending factor (-)
$\Gamma_\epsilon$	$\epsilon$ blending parameter (-)
$\epsilon$	Turbulent dissipation rate ( $\text{m}^2 \text{s}^{-3}$ )
$\epsilon_{visc}$	Turbulent dissipation rate in viscous sub-layer ( $\text{m}^2 \text{s}^{-3}$ )
$\epsilon_{visc}$	Turbulent dissipation rate in log-law layer ( $\text{m}^2 \text{s}^{-3}$ )
$\lambda$	Thermal conductivity ( $\text{W m}^{-1} \text{K}^{-1}$ )
$\mu_t$	Turbulent viscosity ( $\text{Ns/m}^2$ )
$\varphi_{f, muscl}$	Quantity computed with MUSCL numerical scheme (-)
$\varphi_{f, rcd}$	Quantity reconstructed through central differences discretization (-)
$\varphi_{f, ru}$	Quantity computed through second-order upwind discretization (-)
$\omega_i^+$	Production part of the chemical source term ( $\text{kg s}^{-1} \text{m}^{-2}$ )
$\omega_i^-$	Consumption part of the chemical source term ( $\text{kg s}^{-1} \text{m}^{-2}$ )
$\dot{\omega}_j$	Net production rate of species $j$ ( $\text{mol m}^{-3} \text{s}^{-1}$ )
Abbreviations	
AMR	Adaptive Mesh Refinement
FGM	SAGE detailed chemical kinetics solver
LES	Large Eddy Simulation
MAPE	Mean Absolute Percentage Error
MUSCL	Monotonic Upstream-centred Scheme for Conservation Laws
RANS	Reynolds Averaged Navier Stokes
SAGE	SAGE detailed chemical kinetics solver
SSG-RSM	Speziale-Sarkar-Gatski Reynolds Stress Model
Std k- $\epsilon$	Standard 2-equations k- $\epsilon$

## References

1. Tekin, N.; Ashikaga, M.; Horikawa, A.; Funke, H. Enhancement of fuel flexibility of industrial gas turbines by development of innovative hydrogen combustion system. *Rep. Gas Turbines* **2018**, *2*, 18–22.
2. Enagi, I.I.; Al-attab, K.A.; Zainal, Z.A. Combustion chamber design and performance for micro gas turbine application. *Fuel Process. Technol.* **2017**, *166*, 258–268. [[CrossRef](#)]
3. Dovizio, D.; Salehi, M.M.; Devaud, C.B. RANS simulation of a turbulent premixed bluff body flame using conditional source-term estimation. *Combust. Theory Model.* **2013**, *17*, 935–959. [[CrossRef](#)]
4. Burke, S.P.; Schumann, T.E.W. Diffusion Flames. *Ind. Eng. Chem.* **1928**, *20*, 998–1004. [[CrossRef](#)]
5. Bilger, R.W.; Stårner, S.H. A simple model for carbon monoxide in laminar and turbulent hydrocarbon diffusion flames. *Combust. Flame* **1983**, *51*, 155–176. [[CrossRef](#)]
6. Peters, N. Laminar flamelet concepts in turbulent combustion. *Symp. Combust.* **1986**, *21*, 1231–1250. [[CrossRef](#)]

7. Masri, A.R.; Dibble, R.W.; Barlow, R.S. Raman-rayleigh measurements in bluff-body stabilised flames of hydrocarbon fuels. *Symp. Combust.* **1992**, *24*, 317–324. [[CrossRef](#)]
8. Masri, A.R.; Dally, B.B.; Barlow, R.S.; Carter, C.D. The structure of the recirculation zone of a bluff-body combustor. *Symp. Combust.* **1994**, *25*, 1301–1308. [[CrossRef](#)]
9. Masri, A.R.; Kelman, J.B.; Dally, B.B. The instantaneous spatial structure of the recirculation zone in bluff-body stabilized flames. *Symp. Combust.* **1998**, *27*, 1031–1038. [[CrossRef](#)]
10. Benim, A.C.; Pfeiffelmann, B. Comparison of combustion models for lifted hydrogen flames within RANS framework. *Energies* **2019**, *13*, 152. [[CrossRef](#)]
11. Yuan, Y.; Zeng, Q.; Yao, J.; Zhang, Y.; Zhao, M.; Zhao, L. Improving blowout performance of the conical swirler combustor by employing two parts of fuel at low operating condition. *Energies* **2021**, *14*, 1681. [[CrossRef](#)]
12. Li, G.; Naud, B.; Roekaerts, D. Numerical investigation of a bluff-body stabilised nonpremixed flame with differential reynolds-stress models. *Flow Turbul. Combust.* **2003**, *70*, 211–240. [[CrossRef](#)]
13. Dally, B.B.; Fletcher, D.F.; Masri, A.R. Flow and mixing fields of turbulent bluff-body jets and flames. *Combust. Theory Model.* **1998**, *2*, 193–219. [[CrossRef](#)]
14. Syred, N. A review of oscillation mechanisms and the role of the precessing vortex core (PVC) in swirl combustion systems. *Prog. Energy Combust. Sci.* **2006**, *32*, 93–161. [[CrossRef](#)]
15. Aerospace, Mechanical and Mechatronic Engineering. Available online: <https://web.aeromech.usyd.edu.au/thermofluids/swirl.php> (accessed on 8 April 2021).
16. Lübcke, H.; Schmidt, S.; Rung, T.; Thiele, F. Comparison of LES and RANS in bluff-body flows. *J. Wind Eng. Ind. Aerodyn.* **2001**, *89*, 1471–1485. [[CrossRef](#)]
17. Dally, B.B.; Masri, A.R.; Barlow, R.S.; Fiechtner, G.J. Instantaneous and mean compositional structure of bluff-body stabilized nonpremixed flames. *Combust. Flame* **1998**, *114*, 119–148. [[CrossRef](#)]
18. Dally, B.B.; Masri, A.R.; Barlow, R.S.; Fiechtner, G.J.; Fletcher, D.F. Measurements of no in turbulent non-premixed flames stabilized on a bluff body. *Symp. Combust.* **1996**, *26*, 2191–2197. [[CrossRef](#)]
19. Barlow, R.S.; Fiechtner, G.J.; Chen, J.Y. Oxygen atom concentrations and no production rates in a turbulent H<sub>2</sub>/N<sub>2</sub> jet flame. *Symp. Combust.* **1996**, *26*, 2199–2205. [[CrossRef](#)]
20. Van Leer, B. Towards the ultimate conservative difference scheme. V. A second-order sequel to Godunov's method. *J. Comput. Phys.* **1979**, *32*, 101–136. [[CrossRef](#)]
21. Senecal, P.K.; Pomraning, E.; Richards, K.J.; Briggs, T.E.; Choi, C.Y.; McDavid, R.M.; Patterson, M.A. Multi-dimensional modeling of direct-injection diesel spray liquid length and flame lift-off length using cfd and parallel detailed chemistry. *SAE Tech. Pap.* **2003**. [[CrossRef](#)]
22. GRI-Mech 3.0. Available online: <http://combustion.berkeley.edu/gri-mech/version30/text30.html> (accessed on 8 April 2021).
23. Van Oijen, J.A.; De Goey, L.P.H. Modelling of premixed laminar flames using flamelet-generated manifolds. *Combust. Sci. Technol.* **2000**, *161*, 113–137. [[CrossRef](#)]
24. CRECK Modeling. Available online: <http://creckmodeling.chem.polimi.it/menu-kinetics/menu-kinetics-detailed-mechanisms/107-category-kinetic-mechanisms/400-mechanisms-1911-c1-c3-ht-nox> (accessed on 8 April 2021).
25. Venkatakrisnan, V. On the accuracy of limiters and convergence to steady state solutions. In Proceedings of the 31st Aerospace Sciences Meeting, Reno, NV, USA, 11–14 January 1993.
26. Turns, S.R. *An Introduction to Combustion Concepts and Applications*, 3rd ed.; McGraw Hill: New York, NY, USA, 2012; pp. 183–219.
27. Benim, A.C.; Pfeiffelmann, B.; Ocloń, P.; Taler, J. Computational investigation of a lifted hydrogen flame with LES and FGM. *Energy* **2019**, *173*, 1172–1181. [[CrossRef](#)]
28. Pope, S.B. An explanation of the turbulent round-jet/plane-jet anomaly. *AIAA J.* **1978**, *16*, 279–281. [[CrossRef](#)]
29. McGuirk, J.J.; Rodi, W. The calculation of three-dimensional turbulent free jets. *Turbul. Shear Flows* **1979**, 71–83. [[CrossRef](#)]
30. Song, Y.; Marrodán, L.; Vin, N.; Herbinet, O.; Assaf, E.; Fittschen, C.; Stagni, A.; Faravelli, T.; Alzueta, M.U.; Battin-Leclerc, F. The sensitizing effects of NO<sub>2</sub> and NO on methane low temperature oxidation in a jet stirred reactor. *Proc. Combust. Inst.* **2019**, *37*, 667–675. [[CrossRef](#)]